

Wide Range Refractive Index Sensor Using a Birefringent Optical Fiber

Moutusi De (✉ demoutusi@gmail.com)

Indian School of Mines

Vinod Kumar Singh

Optical Fiber Laboratory, Department of Physics, Indian Institute of Technology (ISM), Dhanbad 826004, India

Original Research

Keywords: Surface plasmon resonance, titanium-di-oxide, optical sensor, photonic crystal fiber, birefringence

Posted Date: February 4th, 2021

DOI: <https://doi.org/10.21203/rs.3.rs-172462/v1>

License: © ⓘ This work is licensed under a Creative Commons Attribution 4.0 International License.

[Read Full License](#)

Version of Record: A version of this preprint was published at Optical and Quantum Electronics on April 4th, 2021. See the published version at <https://doi.org/10.1007/s11082-021-02847-6>.

Wide range refractive index sensor using a birefringent optical fiber

Moutusi De and Vinod Kumar Singh*

*Optical Fiber Laboratory, Department of Physics, Indian Institute of Technology (ISM), Dhanbad
826004, India*

**Mail id: vksingh@iitism.ac.in*

Abstract: In this article, an efficient high birefringent D-shaped photonic crystal fiber (HB-D-PCF) plasmonic refractive index sensor is reported. It is able to work over a long low refractive index (RI) analyte range from 1.29 to 1.36. This modified simple structured hexagonal PCF has high birefringence in the near-infrared region. A thin gold film protected by a titanium dioxide (TiO₂) layer is deposited on the D-surface of the PCF which acts as surface plasmon active layer. The sensor consists of an analyte channel on the top of the fiber. The performance of the HB-D-PCF is analyzed based on finite element method (FEM). Both wavelength and amplitude interrogation techniques are applied to study the sensing performance of the optimized sensor. Numerical results show wavelength and amplitude sensitivity of 9245nm/RIU and 1312 RIU⁻¹ respectively with high resolution. Owing to the high sensitivity, long range sensing ability as well as spectral stability the designed HB-D-PCF SPR sensor is a potential candidate for water pollution control, glucose concentration testing, biochemical analyte detection as well as portable device fabrication.

Keywords: Surface plasmon resonance; titanium-di-oxide; optical sensor; photonic crystal fiber; birefringence.

1. Introduction

In the current century, demand for portable, lightweight, long-range, highly sensitive sensors are in peak due to the faster technical development. To satisfy this need intense research work is being performed in the field of photonic crystal fiber (PCF) incorporated optical sensors. PCFs are advantageous over other waveguides due to its great structural flexibility, advantageous optical properties as well as light manipulating capability (De and Singh 2019a; Maji and Chaudhuri 2014; Russell 2003). Based on these charming properties many PCF sensors are reported which are well responding in the field of physical and analyte sensing (De et al. 2019; Pinto and Lopez-Amo 2012). On the other hand, surface plasmon resonance (SPR) is a unique optical phenomenon. In which free electrons at metal-dielectric interface got oscillated by the p-polarized light. Also, maximum energy transfer takes place from the fiber guided mode to the surface plasmon mode when frequency of both these modes are same. This is the resonance frequency which significantly got shifted with changing environment (Islam et al. 2019; Rifat et al. 2016c). So, when this delicate SPR phenomenon is combined with the PCF then the response of these sensors improvised several times in comparison to the non-SPR PCF sensors (Dora Juan 2017). Though PCF is not the first optical element with which plasmonic metals were combined. Firstly invented bulky and less responding prism-based SPR sensors (Raether 1968) were left behind by the optical fiber using SPR sensors. With time, structural and material selection limitation of the standard optical fiber becomes the barrier in its sensitivity enhancement. Then SPR based PCF sensors take the optical sensing technology to a new height (Dora Juan 2017) in the last decade.

For the fabrication of SPR based PCF sensor both internal and external sensing approaches have been applied (Akowuah et al. 2012; Dora Juan 2017). In the case of internal sensing approach air holes of PCF are selectively coated with plasmonic metal as well as filled with analyte (Akowuah et al. 2012). But for external sensing approach both plasmonic metal coating and analyte are situated at the outer surface of PCF (Rifat et al. 2016a). If a comparison is drawn in between these two techniques external sensing is more suitable for real-time applications and mass production of PCF-SPR sensors. As, plasmonic metal layer deposition and its thickness control, analyte filling, probe reuse are more accessible in this case (Dora Juan 2017). Many external plasmonic layers incorporated PCF sensors are reported till date, like, D-shape sensor (An et al. 2018), slotted sensor (Akowuah et al. 2012), flat fiber sensor (Rifat et al. 2016d), micro channel consisting sensors (Liu et al. 2017b) etc. It is prominently noticeable that most of these sensors have high sensitivity and spectral stability in the RI range of 1.40-1.46 due to the less RI discrepancy between the analyte and background material which is silica in most of the cases. But when the analyte RI is far less than the background material then confinement of propagating mode is less affected by the external analyte change resulting in inadequate response to the surrounding changes (Dora Juan 2017). To date, several PCF-SPR low RI sensors are reported. In 2017 Liu *et al.* reported two open-ring channels consisting PCF based SPR sensor (Liu et al. 2017b) which has a sensitivity of 5500nm/RIU in the RI range 1.23-1.29. Though this sensor is responding well toward the analyte change but double-side polishing of the PCF is a troublesome job as well as it makes the probe more fragile. Also, this sensor is operating in the mid-infrared range. Optical sources in this range are not easily available. Next year, Dash *et al.* proposed a micro channel consisting PCF based SPR sensor (Dash et al. 2018) of sensitivity 5000nm/RIU in the RI range 1.32-1.34. Though this structure is less fragile in nature but both sensitivity as well as responding analyte range are limited. After that Islam *et al.* proposed two plasmonic strips consisting birefringent PCF based plasmonic sensor (Islam et al. 2019) which has a sensitivity of 111000nm/RIU in the RI range 1.33-1.43. Though previously mentioned sensor is showing very high sensitivity but its spectral stability is inferior. For real-time applicability of a sensor not only high sensitivity but also its spectral stability matters. Very recently, Wang et al. reported a polarization independent PCF using SPR sensor (Wang et al. 2019b) in 1.20-1.33 RI range with sensitivity 7738nm/RIU. Though it has good sensitivity but its internal structure is very complicated. Also, there are multiple SPR peaks due to the higher order mode coupling. It may create problem during suspected analyte detection.

From a vast literature survey we have concluded that though a large number of D-shaped fiber sensor have reported till today. But a simple structured, long ranged, bio-compatible sensor is still in need. Considering this fact, based on external sensing approach a HB-D-PCF SPR sensor is designed and analyzed for a long low RI analyte region. The D-surface of this fiber probe is coated with active gold and titanium-di-oxide (TiO₂) layers. Using the commercial COMSOL Multiphysics software (FEM), for different active layer thickness coupling conditions and loss spectrum are numerically investigated to achieve the optimized sensor structure. Also, performance of the optimized structure is studied thoroughly based on the wavelength and amplitude interrogation techniques. Mostly incomplete coupling is observed between the fundamental core mode and fundamental SPP mode in the analyte RI range 1.29-1.36. For this sensor maximum wavelength and amplitude sensitivity are found to be 9245nm/RIU and 1312 RIU⁻¹ respectively with high resolution. The advantage of the proposed HB-D-PCF is that it shows high birefringence in the near-infrared region. This helps in manipulating the core guiding light toward the D surface, as a result more interaction with the analyte. Also, due to its moderate propagation loss it is suitable in fabricating a practically realizable sensing probe. As the sensor is operating in near-infrared region, the penetration depth of the evanescent wave and its interaction with the analyte are more in comparison to the visible region.

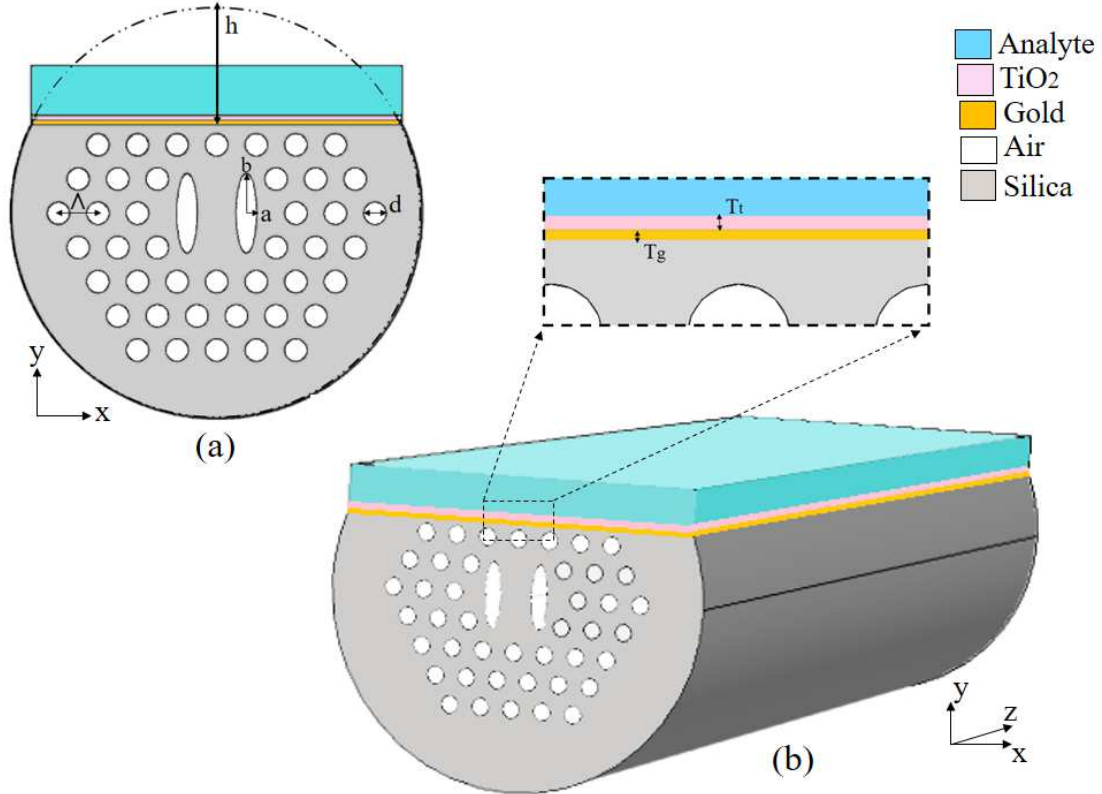


Fig.1. (a) Schematic of the proposed HB-D-PCF; (b) 3D view of the HB-D-PCF sensor

2. Structure design and numerical modeling

The schematic of the designed HB-D-PCF sensor and its 3D view are depicted in Fig. 1. (a) and (b). Air holes are distributed in a hexagonal manner in the cladding region of the PCF. Also, there are two large elliptical air holes around the core. These elliptical holes are promoting the birefringence of the fiber. For this structure, distance between two successive air holes i.e. pitch, circular air hole diameter and eccentricity of the elliptical air holes are $2.00\mu\text{m}$, $1.10\mu\text{m}$ and 0.25 respectively. The area of each elliptical hole is $3.14\mu\text{m}^2$. This HB-D-PCF is made of silica and all holes are filled with air. **Optimization of the previously mentioned structural parameters can be found in detail in our another publication (De and Singh 2019b).** In this work we used the same PCF with modification for further study. This PCF can be considered as a strong competitor of the **commercially available PCF PM-1550** by Thorlabs. Many sensors and interferometers are reported based on this PM-1550 PCF. Similarly, our designed PCF can also be used for fabricating versatile PCF sensors. Incorporation of the plasmonic metal layer on the polished surface of this HB-D-PCF and its application as a low RI analyte sensor is one of them. In our designed HB-D-PCF plasmonic sensor the basic fiber is polished and then the polished surface is coated with thin gold and titanium dioxide (TiO_2) layers respectively. On top of these active layers suspected analyte is placed. Polishing depth from the surface of the fiber, gold layer thickness and TiO_2 layer thickness are denoted by h , T_g and T_t respectively. Gold is a well-known chemically stable plasmonic metal. For this structure, high RI transparent TiO_2 layer protects the gold layer from corrosion as well as enhances the coupling between the evanescent waves of core guided light and external analyte. To realize this HB-D-PCF sensing probe practically, it is suggested to incorporate a thin ($\leq 5\text{nm}$) TiO_2 layer between the fiber (silica) and gold layer. This ultra-thin TiO_2 layer is incorporated as an adhesive layer in spite of weaker adhesion in comparison to

commonly used Cr and Ti coating (Aouani et al. 2009) because of its advantageous spectral tenability over previously mentioned materials (Jiao et al. 2009). In our calculation, it is incorporated as a part of the upper TiO₂ tuning layer to reduce the computational time. Moreover, the TiO₂ layer brings down the operating wavelength as well as SPR frequency in the near-infrared region. It is advantageous in several aspects e.g. infrared light has deeper penetration of SPW evanescent tail as a result sensitivity enhancement and wider availability of infrared sources and detectors (Ziblat et al. 2006). For this HB-D-PCF analyte RI is varied from 1.29 to 1.36. Also, the sensor structure is optimized based on polishing depth and layer thickness which are discussed in section 5.1. RI of air is 1. Material dispersion of silica is considered throughout the simulation using the Sellmeier equation (De and Singh 2019a). The complex dielectric constant of gold is taken into account in this simulation as per Johnson and Christy data (P. B. Johnson and Christy 1972). The dispersion relation of TiO₂ is taken into account as per Mishra *et al.* (Mishra and Mishra 2015),

$$\epsilon_{TiO_2} = 5.913 + \frac{0.2441}{\lambda^2 - 0.0843} \quad (1)$$

Here, λ is the wavelength of core guided mode.

FEM based numerical simulation is used to analyze the sensor under study. Also, an anisotropic perfectly match layer is placed around the fiber to reduce radiation loss. During numerical analysis cross-section of the sensor is discretized into small triangular element. Then Maxwell's em equations are applied at each element. Combining all these solutions global matrix is formed and finally effective refractive indices (n_{eff}) of different modes are computed. During this simulation 26503 domain elements, 2289 boundary elements and 175387 degrees of freedoms are solved.

3. Fabrication prospects

The designed HB-D-PCF is practically realizable in dimension. This hexagonal fiber can be fabricated using developed stack and draw technique (Russell 2003) and laser drilling technique (Becker et al. 2013). The fused preform technique can be applied to realize the elliptical air holes (Falkenstein et al. 2004). Also, laser drilling technique (Becker et al. 2013) and 3D printing technique (Rosales et al. 2020) can be applied to build the preform. Then using this preform fiber can be fabricated by developed stack and draw technique. The D-surface of this structure can be achieved by careful polishing of the fiber surface (An et al. 2018; Dora Juan 2017). For this HB-D-PCF sensor, gold and TiO₂ layers are externally coated. So, this structure is free from internal or selective coating complexity. The gold and TiO₂ layers can be deposited on the D-surface by applying the sputtering technique (Armelaio et al. 2005) and chemical method (Akhilesh Kumar Pathak, Vanita Bhardwaj, Rahul Kumar Gangwar, Moutusi De 2016) respectively. Additionally, few microliter analyte is needed to pour on the top of the sensing probe. Fig. 2 depicts a recommended experimental setup. Free space coupling (Heng et al. 2016) or recently developed connector technique (Morishima et al. 2018) can be applied to launch light at the probe and then routed to the OSA (optical spectrum analyzer) (Wu et al. 2017). Considering all these aspects and currently available fiber technology, we authors are hopeful regarding the real-time applicability of this sensor. It should be kept in mind that polishing of the PCF should be performed very carefully to avoid the damage of the probe. Also, after the fabrication the probe should be attached with a rigid platform to avoid the deterioration of the sensor performance.

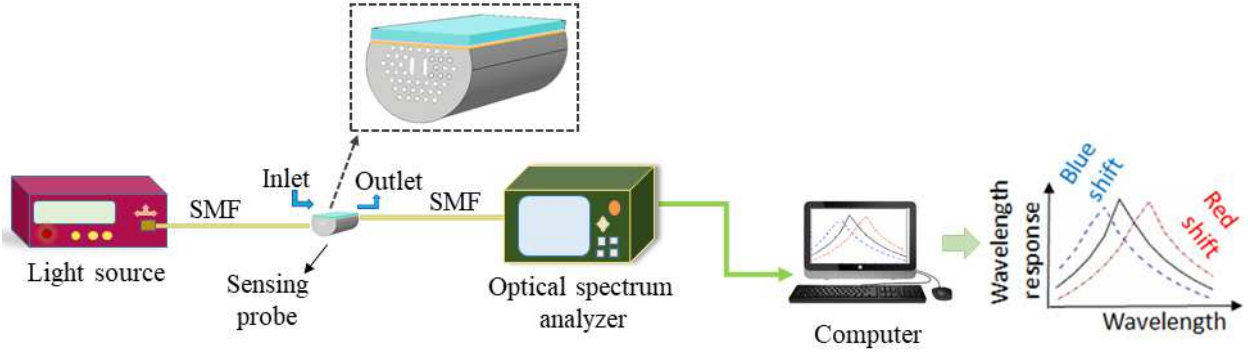


Fig. 2. Schematic diagram of the proposed experimental setup

4. Working principle of the proposed SPR sensor and dispersion relation

For this probe, light is propagating along z-direction and all modal analysis are performed at the x-y plane (Fig.1.a). The working principle of this HB-D-PCF is governed by coupled mode theory (CMT). As per this theory core guided mode and SPP mode gets coupled at a particular frequency when their effective refractive indices (n_{eff}) are matched. It is also known as the phase matching point (Dora Juan 2017). Here, it is worthy of mentioning that throughout all analysis y polarized fundamental core mode is considered because this mode breaks the symmetry of the structure as the plasmonic layer is situated in the y-direction. As a result better interaction takes place between evanescent wave of y polarized core mode and analyte in comparison to the x polarized mode in the infrared region (An et al. 2018; Dora Juan 2017). For this sensor, energy coupling takes place from the core mode to the fundamental surface plasmon polarization (SPP) mode and maximum loss appears in the core mode at the resonance wavelength. This loss spectra is highly dependent on structural parameters, active layers thickness and the surrounding environment. Confinement loss of both core guided mode and SPP mode can be formulated as,

$$\alpha(\text{dB/cm}) = 8.686 \times \frac{2\pi}{\lambda} \text{Im}(n_{\text{eff}}) \times 10^4 \quad (2)$$

here, $\text{Im}(n_{\text{eff}})$ is the imaginary part of effective RI (Gangwar and Singh 2017).

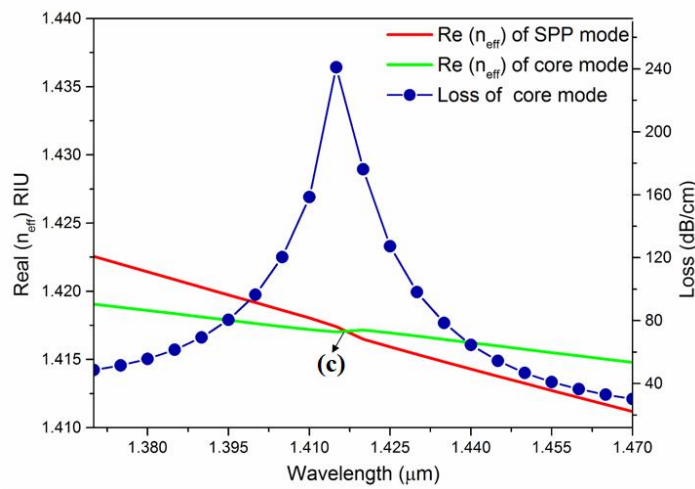


Fig.3

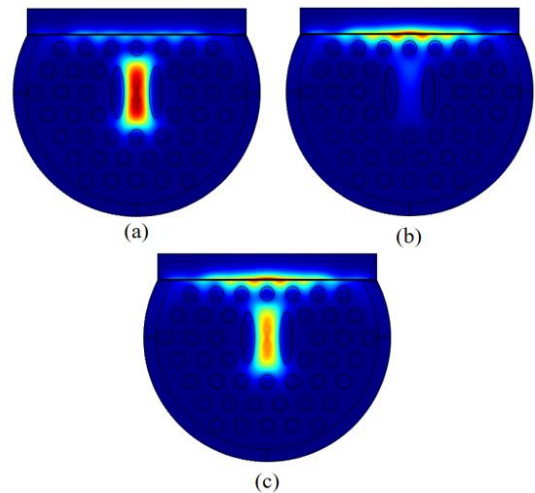


Fig.4

Fig. 3 Dispersion relations of core mode and SPP mode for designed HB-D-PCF for $n_a=1.33$.
Fig. 4 electric field distribution of (a) core guided mode, (b) SPP mode and (c) coupled mode.

Fig.3 shows the dispersion repletion of core mode and SPP mode for the optimized structure at $n_a=1.33$. In Fig.3 $\text{Re}(n_{\text{eff}})$ of core mode, $\text{Re}(n_{\text{eff}})$ of SPP mode and loss of core mode variation with changing wavelength are denoted by solid green line, solid red line and blue line with circle respectively. It can be observed from Fig.3 that at $1.415\mu\text{m}$ propagating wavelength $\text{Re}(n_{\text{eff}})$ of core mode and SPP mode are matched and coupling takes place between them. At this particular wavelength loss of the core mode is maximum and it is known as SPR wavelength. Fig. 4 represents the electrical field distribution of core and SPP modes for $n_a=1.33$. Fig.4. (a) and (b) are the core and SPP mode at $1.380\mu\text{m}$ wavelength (away from coupling) and Fig.4. (c) is the coupled mode at $1.415\mu\text{m}$ wavelength. It can be visualized that at coupling wavelength electric field is prominently present both in core and SPP mode. The SPR wavelength suffers a significant shift with the changing environment. So, wavelength sensitivity can be calculated by tracking the SPR wavelength shift as follows,

$$S_\lambda (nm/RIU) = \frac{\Delta\lambda_{\text{peak}}}{\Delta n_a} \quad (3)$$

here, $\Delta\lambda_{\text{peak}}$ is the SPR wavelength shift for Δn_a , analyte RI change.

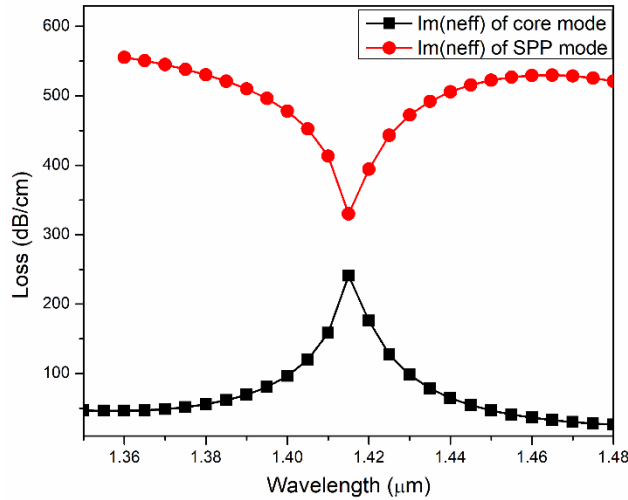


Fig.5 Incomplete coupling of core mode and SPP mode for the designed HB-D-PCF for $n_a=1.33$.

Not only the strength of coupling but also the coupling nature between core and SPP mode can be explained well based on CMT (Fan et al. 2015; Ma et al. 2013). Following this theory two coupled modes can be presented as follows,

$$\frac{dE_1}{dz} = -i\beta_1 E_1 + i\mathcal{K}_{12} E_2 \quad (4)$$

$$\frac{dE_2}{dz} = -i\beta_2 E_2 + i\mathcal{K}_{21} E_1 \quad (5)$$

here, β_1 and β_2 are propagation constants, $E_1=A \exp(i\beta z)$ and $E_2=B \exp(i\beta z)$ are fields associated with the core and SPP mode. z and \mathcal{K} are the propagation length and coupling strength respectively. By substituting E_1 and E_2 in the solution of Eq. (4) and (5), it can be written as,

$$\beta_{\pm} = \beta_{\text{ave}} \pm \sqrt{\delta^2 + \mathcal{K}^2} \quad (6)$$

here, $\beta_{\text{ave}} = (\beta_1 + \beta_2)/2$ and $\delta = (\beta_1 - \beta_2)/2$. β_1 , β_2 and δ all are complex quantities with $\delta = \delta_r + i\delta_i$. When, $\delta_i > \mathcal{K}$, β_+ and β_- have same real part and different imaginary part. In this case an incomplete coupling takes place. On the other hand, complete coupling takes place in a converse case. Fig.5 depicts the incomplete coupling

at $n_a=1.33$ for the designed HB-D-PCF. The coupling nature over the entire analyte range will be discussed in section 5.2.

5. Results and discussion

5.1. Influence of structural parameters on loss spectrum and optimization

The PCF shows high birefringence throughout the near-infrared region (as shown in Fig.6 (De and Singh 2019a)) and it suffers increment with increasing wavelength. It has birefringence of 3.93×10^{-3} at $1.55 \mu\text{m}$ wavelength. The presence of broader passage along y-direction is the reason behind more modal spreading as well as high birefringence (De and Singh 2019a). The effect of polishing depth and active layers thickness on loss spectrum are investigated in detail to design an optimal performing HB-D-PCF sensor, and findings are depicted in Fig.7. During this process parameters are optimized one at a time. With changing parameters losses of core guided modes are calculated using Eq. (2).

For a SPR sensor, thickness of the plasmonic metal layer is a crucial parameter. Because SPP wave as well as modal coupling are strongly dependent on this layer thickness. Fig. 7(a) shows the variation of loss spectra for different polishing depths when $T_g=T_t=40\text{nm}$. For increasing h from $3.94 \mu\text{m}$ to $4.39 \mu\text{m}$ with an iteration of $0.15 \mu\text{m}$, SPR wavelength suffers blue shift (indicated with blue arrow) from $1.269 \mu\text{m}$ to $1.165 \mu\text{m}$ with varying loss peak. In the beginning, loss started to increase with increasing polishing depth because deeper polishing allows more interaction between core mode and external analyte. In this case loss is maximum for $h=4.24 \mu\text{m}$ with sharp loss peak. But when the fiber is polished more then there is a coupling tendency between core mode and first order SPP mode (blue dash-dot line). As a result, loss peak of fundamental mode decreases and sensitivity becomes less. Also, very deep polishing makes the fiber fragile and coupled modes desultory. So, $h=4.24 \mu\text{m}$ is chosen to get a well-responding sensing probe. It can also be observed that response of the probe is highly sensitive to the polishing depth. So, special care should be taken during fabrication.

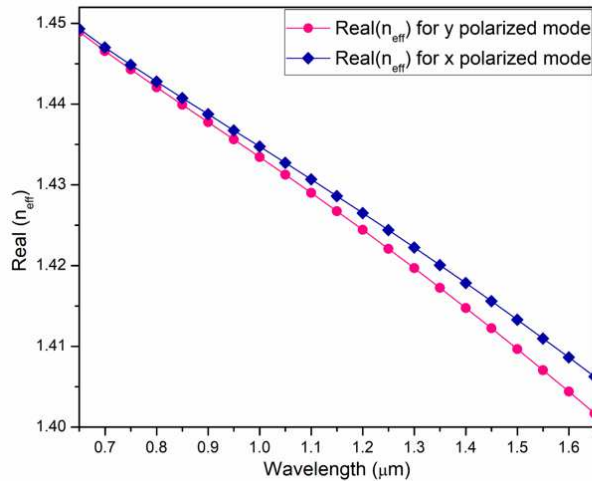


Fig.6

Fig.6 Real (n_{eff}) variation for both x and y polarized mode with changing wavelength for optimized unpolished PCF structure (De and Singh 2019a). Fig.7. (a) Loss spectrum of the designed HB-D-PCF sensor with changing h at $n_a=1.33$.

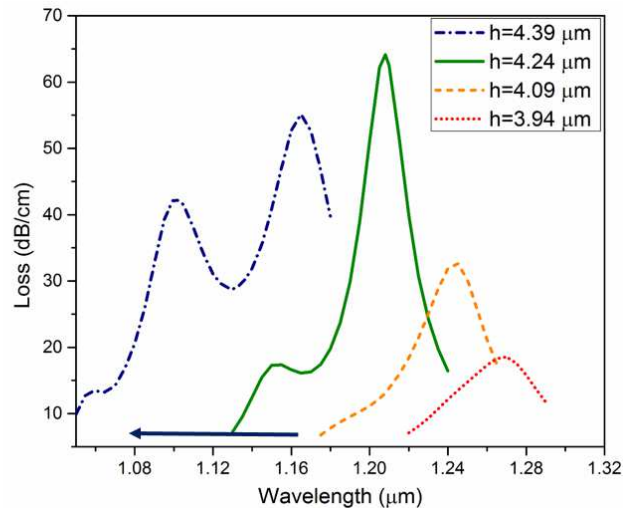


Fig. 7(a)

Fig. 7(b) shows loss spectra of core mode for varying T_g with $h=4.24 \mu\text{m}$ and $T_t=40\text{nm}$. For increasing T_g from 35nm to 55nm with an iteration of 5nm , SPR wavelength suffers red shift (indicated with red arrow)

from 1.160 μm to 1.274 μm . One fact is noticeable in Fig. 7(b) that resonance loss is maximum for 40nm thick gold layer with a most sharp peak among all. It can be explained as, for a well responding SPR sensing probe the plasmonic layer has an optimum thickness. When the plasmonic layer is too thin then it is not able to accommodate a sufficient number of SPP modes due to high mechanical damping. contrarily when the plasmonic layer is too thick core mode is unable to interact with external analyte properly or penetration depth is limited i.e. plasmonic damping (De and Singh 2020). So, the optimum gold layer thickness is chosen as 40nm for this HB-D-PCF sensor.

Then the effect of T_t on fundamental core mode loss is studied in detail with $h=4.24\mu\text{m}$ and $T_g=40\text{nm}$ as shown in Fig. 7(c). For increasing T_t from 35nm to 60nm with an iteration of 5nm, SPR wavelength suffers red shift (indicated with red arrow) from 1.140 μm to 1.576 μm with loss increment at the beginning. For $T_t=50\text{nm}$, loss curve is very sharp with highest loss. Also, higher order resonance loss peak is much lower than the fundamental core loss peak. It can be noticed that with increase T_t resonance loss peak started to increase until the other higher order loss peak appears prominently. The reason behind this is the TiO_2 layer enhances the mode coupling as well as light analyte interaction. But wider T_t screens core guided light from analyte. So, $T_t=50\text{nm}$ is chosen as optimized TiO_2 layer thickness.

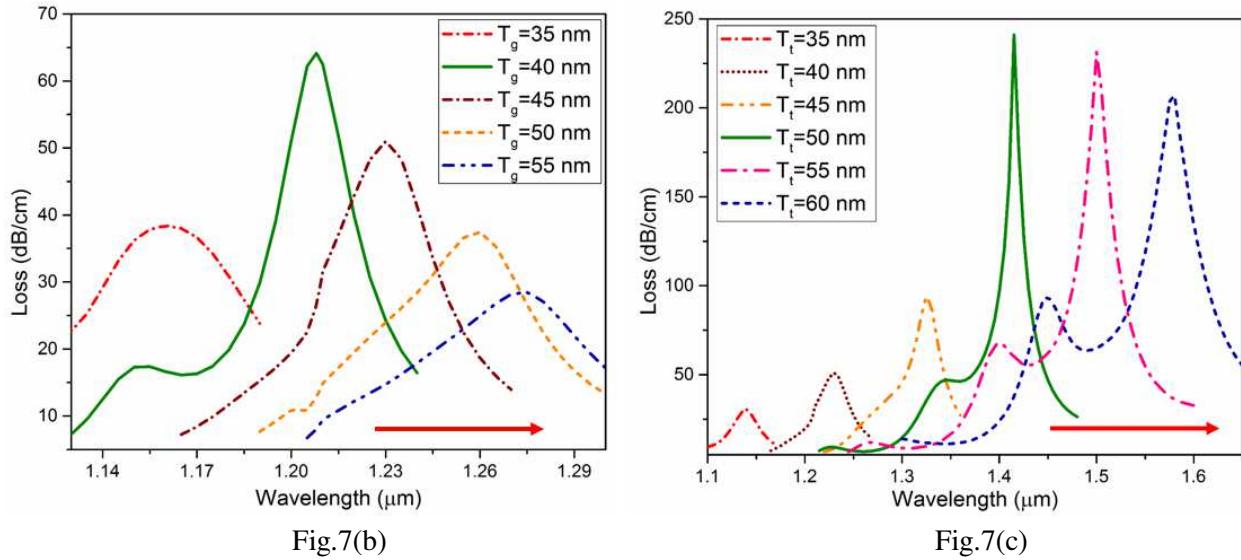


Fig. 7 Loss spectrum of the designed HB-D-PCF sensor with changing (b) T_g and (c) T_t at $n_a=1.33$.

5.2. Performance analysis

The loss spectrum of the optimized HB-D-PCF SPR sensor having structural parameters $h=4.24\mu\text{m}$, $T_g=40\text{nm}$ and $T_t=50\text{nm}$ are depicted in Fig.8 (a). The proposed sensor is performing best in the analyte RI (n_a) range 1.29 to 1.36. For an analyte having RI below this range modes become desultory. Also, for an analyte above this RI range wavelength response is poor. It can be observed from Fig.8 (a) that SPR wavelength suffers a red shift from 1.220 to 1.672 with increasing n_a (indicated with red arrow). The reason behind this is that n_{eff} of core mode and SPP mode are close to RI of silica fiber and n_a respectively. So, increment in n_a causes red shift of the phase matching point as well as SPR wavelength (De and Singh 2020). It is also noticeable in Fig.8 (a) that loss peak goes through a circle of rising and fall in that particular range. In the beginning, loss suffers increment with increasing n_a and then comes to a maximum of 239dB/cm at 1.415 μm wavelength for $n_a=1.33$. After that, loss starts to decrease with increasing n_a . This is because of the strongest coupling between core mode and SPP mode at $n_a=1.33$ which is also observable in Fig. 10. Throughout the

studied RI range loss is moderate for this sensor which is another attractive feature for its practical implementation. The performance of the optimized HB-D-PCF SPR sensor is summarized in Table-1.

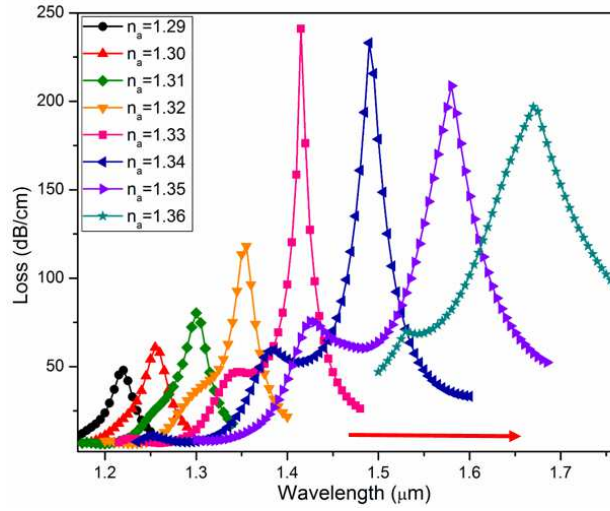


Fig. 8(a)

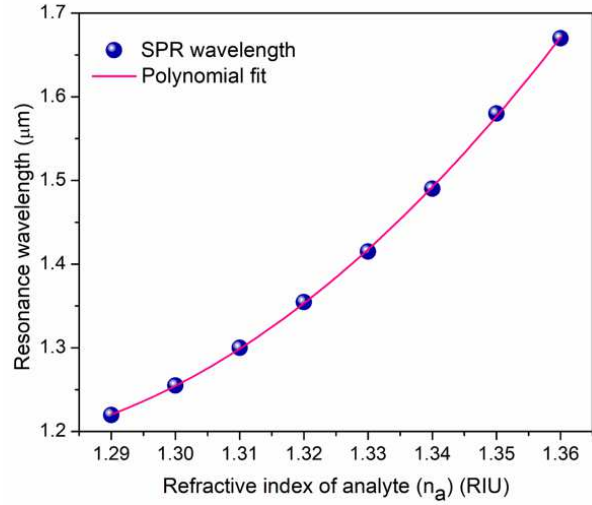


Fig. 8(b)

Fig. 8 (a) Loss spectrum for various analytes, (b) SPR wavelength variation with changing analyte.

Table 1. Performance of the HB-D-PCF SPR sensor for analyte variation

Analyte RI (n_a) (RIU)	SPR wavelength (λ_{peak}) (μm)*	Loss (α) (dB/cm)	S_λ (nm/RIU)	FWHM (nm)
1.29	1.220	48	3535	36
1.30	1.255	61	4490	39
1.31	1.300	80	5467	42
1.32	1.355	118	6035	36
1.33	1.415	239	7520	22
1.34	1.490	232	8978	40
1.35	1.580	209	9245	82
1.36	1.672	198	-	160

* Approximation is made up to three digits after decimal.

SPR wavelength shift with changing n_a is depicted in Fig.8 (b). By applying wavelength interrogation technique on this cure wavelength sensitivity can be calculated using Eq. (3). The highest sensitivity of this sensor is found to be 9245nm/RIU. These observed data points are fitted very well with second-degree polynomial equations with R^2 value 0.9998. The relation between SPR peak and n_a can be presented as follows,

$$\lambda_{peak} = 81.0511 - 126.6890n_a + 50.2362n_a^2 \quad (7)$$

Figure of merits (FOM) (Fan et al. 2015) of this sensor can be calculated as follows,

$$FOM = \frac{S_\lambda}{FWHM} \quad (8)$$

with varying n_a full width at half maximums (FWHM) are presented in Table-1. For this HB-D-PCF SPR sensor FOM can reach up to 342 at $n_a=1.33$ which is reasonably high. In this designed fiber, asymmetry is induced around the core by incorporating two elliptical air holes next to the core. Due to this a broader passage way is created along y direction in comparison to x direction. Here, more interaction takes place

between fiber guided light and analyte because active layers (Au and TiO₂) are situated on polished surface along y direction. As a result sensitivity got enhanced (Dash and Jha 2014).

Also the amplitude interrogation technique is applied to investigate the sensitivity of the proposed sensor. This technique is economically beneficial because of the use of a single source. When propagating light suffers loss of $\alpha(\lambda, n_a)$ due to the propagation through a probe length L, its amplitude sensitivity can be defined as (Dash and Jha 2014; Rifat et al. 2015),

$$S_A(\lambda)[RIU^{-1}] = -\frac{1}{\alpha(\lambda, n_a)} \frac{\partial \alpha(\lambda, n_a)}{\partial n_a} \quad (9)$$

Fig. 9 depicts amplitude sensitivity of the proposed sensor in the RI ranging from 1.30 to 1.36. Again red shift is noticeable in this case with increasing n_a (denoted by red arrow). The reason for this shift is previously mentioned. Maximum S_A is found to be 1312RIU⁻¹ with $n_a=1.33$. Also, the coupling characteristics between core mode and SPP mode is presented in Fig. 10. It shows incomplete coupling throughout the studied RI range. So, this HB-D-PCF SPR sensor is advantageous in detecting bio analytes (Merwe 2000).

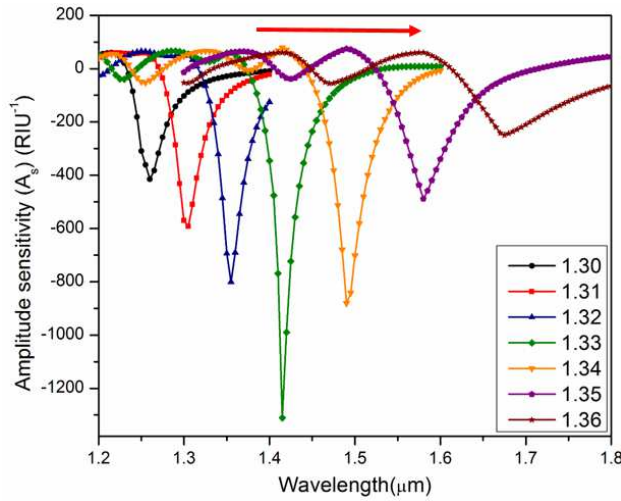


Fig. 9

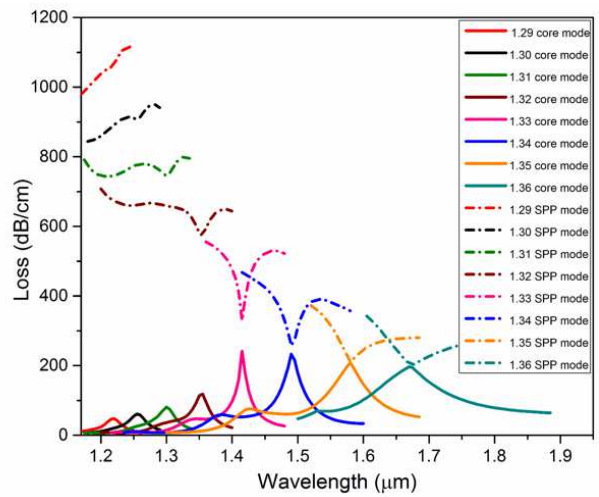


Fig. 10

Fig. 9 Amplitude sensitivity of proposed HB-D-PCF sensor with varying analyte; Fig. 10 Coupling nature in RI range 1.29-1.36.

Resolution shows the minimum detection ability of a sensor which can be calculated using following equation (Rifat et al. 2016d),

$$R = \Delta n_a \times \frac{\Delta \lambda_{min}}{\Delta \lambda_{peak}} RIU \quad (10)$$

In case wavelength interrogation method, R of the HB-D-PCF sensor is 1.08×10^{-5} RIU when $\Delta \lambda_{min}=0.1$ nm and for amplitude interrogation method it is 7.62×10^{-6} RIU for 1% transmission power at the output. The superiority of the proposed HB-D-PCF SPR sensor over other reported literature is presented in Table-2.

Table 2. Performance comparison of the HB-D-PCF SPR sensor

Reported structure	RI Range	Wavelength sensitivity (nm/RIU)	Amplitude sensitivity (RIU ⁻¹)	Resolution (RIU)	FOM	Reported year	Ref.
Internally gold film coated slotted PCF	1.33-1.34	2000	220	5.00×10 ⁻⁵	-	2012	(Akowuah et al. 2012)
Externally graphene-silver layer coated birefringent PCF	1.33-1.36	-	860	4.00×10 ⁻⁵	-	2014	(Dash and Jha 2014)
Externally gold coating two rings hexagonal lattice PCF	1.33-1.37	4000	320	2.50×10 ⁻⁵	-	2015	(Rifat et al. 2015)
Externally gold layer coated modified hexagonal PCF	1.33-1.37	1000	118	1.00×10 ⁻⁴	-	2016	(Rifat et al. 2016c)
Hexagonal PCF externally coated with copper-graphene layer	1.33-1.37	2000	140	5.00×10 ⁻⁵	-	2016	(Rifat et al. 2016b)
Analyte filled diamond ring fiber coated with gold layer from inside	1.33-1.39	6000	508	1.67×10 ⁻⁵	-	2017	(Ng et al. 2018)
Gold nanowire combined with solid core PCF	1.27-1.36	2350	600	2.80×10 ⁻⁵	-	2017	(Liu et al. 2017a)
Rectangular lattice quasi-D-shaped PCF with gold-graphene coating	1.33-1.42	3877	1236	2.58×10 ⁻⁵	-	2018	(An et al. 2018)
Negatively curved air rings consisting of microstructured fiber with external gold coating	1.20-1.34	8892	-	6.54×10 ⁻⁶	-	2019	(Wang et al. 2019a)
Dual channel consisting optical fiber	1.30-1.36	1650			55	2019	(Al. 2019)
Bi-layer coated lossy mode resonance based sensor	1.33-1.38	4400	-	-		2020	(Vivek Semwal and Banshi D. Gupta 2020)
Hollow core graded index optical fiber	1.38-1.49	4350	-	-	149	2020	(Al. 2020)
HB-D-PCF with gold-TiO ₂ coating	1.29-1.36	9245	1312	1.08×10 ⁻⁶	342	2021	Our work

6. Conclusion

An optimized SPR sensor is proposed based on a high birefringent PCF. Its sensing performance as well as coupling nature are investigated in RI range 1.29-1.36 using wavelength and amplitude interrogation techniques. This HB-D-PCF SPR sensor exhibits maximum wavelength and amplitude sensitivity of 9245nm/RIU and 1312RIU⁻¹ respectively. It is able to detect RI change up to the order of 10⁻⁶. Also it shows a high FOM of 342. This moderately lossy SPR sensor is practically realizable using developed stack and draw method and can be a good competitor of commercially available fiber using D-PCF sensors. Long range sensing ability of this complexity free structure is its key advantage over many D-shaped plasmonic

PCF sensors. The promising features of the proposed sensor make it a suitable candidate for integrating with the lab-on-a-fiber technology, developing fiber interferometer as well as fabricating portable biochemical sensing devices.

Acknowledgment: We are thankful to IIT(ISM) Dhanbad for providing all facilities and financial support for this work.

Declarations:

Funding: Not applicable.

Conflict of interest / Competing interest: The authors have no conflict of interest.

Availability of data and material: All data are available.

Code availability: Not applicable.

References:

Akhilesh Kumar Pathak, Vanita Bhardwaj, Rahul Kumar Gangwar, Moutusi De, V.K.S.: Fabrication and characterization of TiO₂ coated cone shaped nano-fiber pH sensor. *Opt. Commun.* 386, (2016).

<https://doi.org/10.1016/j.optcom.2016.11.021>

Akowuah, E.K., Gorman, T., Ademgil, H., Haxha, S., Robinson, G.K., Oliver, J. V.: Numerical analysis of a photonic crystal fiber for biosensing applications. *IEEE J. Quantum Electron.* 48, 1403–1410 (2012).

<https://doi.org/10.1109/JQE.2012.2213803>

Al., R.N. et: Dual channel optical fiber refractive index sensor based on surface plasmon resonance. *Opt. - Int. J. Light Electron Opt.* 186, 194–204 (2019).

<https://doi.org/https://doi.org/10.1016/j.ijleo.2019.04.104>

Al., R.N. et: Hollow-core graded index optical fiber refractive index sensor based on surface plasmon resonance. *Opt. Quantum Electron.* 52, 341 (2020). <https://doi.org/https://doi.org/10.1007/s11082-020-02461-y>

An, G., Li, S., Wang, H., Zhang, X.: Quasi-D-shaped optical fiber plasmonic refractive index sensor. *J. Opt.* 20, 104433-1–5 (2018). <https://doi.org/10.1088/2040-8986/aaaa42>

Aouani, H., Wenger, J., Gérard, D., Rigneault, H., Devaux, E., Ebbesen, T.W., Mahdavi, F., Xu, T., Blair, S.: Crucial role of the adhesion layer on the plasmonic fluorescence enhancement. *ACS Nano.* 3, 2043–2048 (2009). <https://doi.org/10.1021/nn900460t>

Armelaio, L., Barreca, D., Bottaro, G., Bruno, G., Gasparotto, A., Losurdo, M., Tondello, E.: RF-sputtering of gold on silica surfaces: Evolution from clusters to continuous films. *Mater. Sci. Eng. C.* 25, 599–603 (2005). <https://doi.org/10.1016/j.msec.2005.06.007>

Becker, M., Werner, M., Fitzau, O., Esser, D., Kobelke, J., Lorenz, A., Schwuchow, A., Rothhardt, M., Schuster, K., Hoffmann, D., Bartelt, H.: Laser-drilled free-form silica fiber preforms for microstructured optical fibers, (2013)

Dash, J.N., Das, R., Jha, R.: AZO coated microchannel incorporated PCF-based SPR sensor: A numerical analysis. *IEEE Photonics Technol. Lett.* 30, 1032–1035 (2018).

<https://doi.org/10.1109/LPT.2018.2829920>

Dash, J.N., Jha, R.: Graphene-Based Birefringent Photonic Crystal Fiber Sensor Using Surface Plasmon Resonance. *IEEE Photonics Technol. Lett.* 26, 1092–1095 (2014)

De, M., Gangopadhyay, T.K., Singh, V.K.: Prospects of Photonic Crystal Fiber as Physical Sensor: An Overview. *Sensors.* 19, 464 (2019). <https://doi.org/10.3390/s19030464>

De, M., Singh, V.K.: Multi-purpose photonic crystal fiber having advanced optical properties and long sensing range, (2019)(a)

De, M., Singh, V.K.: Multi-purpose photonic crystal fiber having advanced optical properties and long sensing range. *Photonics Nanostructures - Fundam. Appl.* 36, (2019)(b).

<https://doi.org/10.1016/j.photonics.2019.100722>

De, M., Singh, V.K.: Analysis of a highly sensitive flat fiber plasmonic refractive index sensor. *Appl. Opt.* 59, 380–388 (2020). <https://doi.org/10.1364/AO.59.000380>

Dora Juan, J.H. and H.P.H.: Recent advances in plasmonic photonic crystal fiber: design, fabrication and applications. *Adv. Opt. Photonics.* 9, 257–314 (2017). <https://doi.org/10.1364/AOP.9.000257>

Falkenstein, P., Merritt, C.D., Justus, B.L.: Fused preforms for the fabrication of photonic crystal fibers. *Opt. Lett.* 29, 1858 (2004). <https://doi.org/10.1364/OL.29.001858>

Fan, Z., Li, S., Liu, Q., An, G., Chen, H., Li, J., Chao, D., Li, H., Zi, J., Tian, W.: High sensitivity of refractive index sensor based on analyte-filled photonic crystal fiber with surface plasmon resonance. *IEEE Photonics J.* 7, 4800809 (2015). <https://doi.org/10.1109/JPHOT.2015.2432079>

Gangwar, R.K., Singh, V.K.: Highly Sensitive Surface Plasmon Resonance Based D-Shaped Photonic Crystal Fiber Refractive Index Sensor. *Plasmonics.* 12, 1367–1372 (2017).

<https://doi.org/10.1007/s11468-016-0395-y>

Heng, D.O.Z., An, Y.L.I., Hen, E.R.H.U.C., Eibei, B.L.I., Ong, D.E.K., Ei, W.L.I., Ian, J.W.U.: Free-space to few-mode-fiber coupling under atmospheric turbulence. *Opt. Express.* 24, 18739–18744 (2016)

Islam, M.S., Sultana, J., Ahmmed Aoni, R., Habib, M.S., Dinovitser, A., Ng, B.W.-H., Abbott, D.: Localized surface plasmon resonance biosensor: an improved technique for SERS response intensification. *Opt. Lett.* 44, 1134 (2019). <https://doi.org/10.1364/ol.44.001134>

Jiao, X., Goeckeritz, J., Blair, S., Oldham, M.: Localization of near-field resonances in bowtie antennae: Influence of adhesion layers. *Plasmonics.* 4, 37–50 (2009). <https://doi.org/10.1007/s11468-008-9075-x>

Liu, C., Yang, L., Liu, Q., Wang, F., Sun, Z., Sun, T.: Analysis of a Surface Plasmon Resonance Probe Based on Photonic Crystal Fibers for Low Refractive Index Detection. *Plasmonics.* (2017)(a).

<https://doi.org/10.1007/s11468-017-0572-7>

Liu, C., Yang, L., Lu, X., Liu, Q., Wang, F., Lv, J., Sun, T., Mu, H., Chu, P.K.: Mid-infrared surface plasmon resonance sensor based on photonic crystal fibers. *Opt. Express.* 25, 14227 (2017)(b).

<https://doi.org/10.1364/oe.25.014227>

Ma, A., Li, Y., Zhang, X.: Coupled mode theory for surface plasmon polariton waveguides. *Plasmonics.* 8, 769–777 (2013). <https://doi.org/10.1007/s11468-012-9471-0>

Maji, P.S., Chaudhuri, P.R.: Dispersion properties of the square-lattice elliptical-core PCFs Core Square-Lattice PCFs. 2, 1–6 (2014). <https://doi.org/10.11648/j.ajop.20140201.11>

Merwe, P.A. van der: Surface plasmon resonance protein-ligand interactions: a practical approach. Oxford University Press (2000)

Mishra, A.K., Mishra, S.K.: Infrared SPR sensitivity enhancement using ITO / TiO₂ / silicon. *Europhys. Lett.* 112, 10001-p1-5 (2015). <https://doi.org/10.1209/0295-5075/112/10001>

Morishima, T., Shimakawa, O., Ito, J., Shimazu, T., Arai, H., Yokochi, T., Uehara, F., Ohmura, M., Nakanishi, T., Sano, T., Hayashi, T.: Ultra-high-density MCF connector technology. In: OFC. p. W1A.5 (2018)

Ng, W.L., Rifat, A.A., Wong, W.R., Mahdiraji, G.A., Mahamd Adikan, F.R.: A Novel Diamond Ring Fiber-Based Surface Plasmon Resonance Sensor. *Plasmonics.* 13, 1165–1170 (2018).

<https://doi.org/10.1007/s11468-017-0617-y>

P. B. Johnson, Christy, R.W.: Optical constant of the noble metals. *Phys. Rev. B.* 6, 4370–4379 (1972). <https://doi.org/10.1103/PhysRevB.6.4370>

Pinto, A.M.R., Lopez-Amo, M.: Photonic Crystal Fibers for Sensing Applications. *J. Sensors.* 2012, 1–21 (2012). <https://doi.org/10.1155/2012/598178>

Raether, E.K. and H.: Radiative decay of non-radiative surface plasmons excited by light. *Z. Naturforsch. A.* 23, 2135–2136 (1968)

Rifat, A.A., Mahdiraji, G.A., Ahmed, R., Chow, D.M., Sua, Y.M., Shee, Y.G., Adikan, F.R.M.: Copper-graphene-based photonic crystal fiber plasmonic biosensor. *IEEE Photonics J.* 8, (2016)(a).

<https://doi.org/10.1109/JPHOT.2015.2510632>

Rifat, A.A., Mahdiraji, G.A., Ahmed, R., Chow, D.M., Sua, Y.M., Shee, Y.G., Adikan, F.R.M.: Copper-graphene-based photonic crystal fiber plasmonic biosensor. *IEEE Photonics J.* 8, 4800408 (2016)(b).

<https://doi.org/10.1109/JPHOT.2015.2510632>

Rifat, A.A., Mahdiraji, G.A., Shee, Y.G., Shawon, M.J., Adikan, F.R.M.: A Novel Photonic Crystal Fiber Biosensor Using Surface Plasmon Resonance. *Procedia Eng.* 140, 1–7 (2016)(c).

<https://doi.org/10.1016/j.proeng.2015.08.1107>

Rifat, A.A., Mahdiraji, G.A., Sua, Y.M., Ahmed, R., Shee, Y.G., Adikan, F.R.M.: Highly sensitive multi-core flat fiber surface plasmon resonance refractive index sensor. *Opt. Express.* 24, 2485 (2016)(d).

<https://doi.org/10.1364/OE.24.002485>

Rifat, A.A., Mahdiraji, G.A., Sua, Y.M., Shee, Y.G., Ahmed, R., Chow, D.M.: Surface plasmon resonance photonic crystal fiber biosensor : a practical sensing approach. *IEEE Photonics Technology Lett.* 27, 1628–1631 (2015). <https://doi.org/10.1109/LPT.2015.2432812>

Rosales, A.L.C., Velázquez, M.M.A.N., Zhao, X., Sahu, J.K.: Optical fibers fabricated from 3D printed silica preforms. In: *SPIE LASE.*, San Francisco, California, United States (2020)

Russell, P.: *Photonic Crystal Fibres.* Science (80-.). 299, 358–362 (2003)

Vivek Semwal and Banshi D. Gupta: Lossy mode resonance-based highly sensitive fiber optic refractive index sensor using the bilayer of FTO/HfO₂ for operation in the visible region. *J. Opt. Soc. Am. B.* 37 (12), 3841–3849 (2020). <https://doi.org/https://doi.org/10.1364/JOSAB.404670>

Wang, J., Pei, L., Wang, J., Ruan, Z., Zheng, J., Li, J.: Surface plasmon resonance sensor for low refractive index detection based on microstructured fiber. *J. Opt. Soc. Am. B.* 36, 3104 (2019)(a). <https://doi.org/10.1364/josab.36.003104>

Wang, J., Pei, L., Wu, L., Wang, J., Ruan, Z., Zheng, J.: A Polarization-independent SPR sensor based on photonic crystal fiber for low RI detection. *Plasmonics.* (2019)(b). <https://doi.org/10.1007/s11468-019-01054-0>

Wu, T., Shao, Y., Wang, Y., Cao, S., Cao, W., Zhang, F., Liao, C., He, J., Huang, Y., Hou, M., Wang, Y.: Surface plasmon resonance biosensor based on gold-coated side-polished hexagonal structure photonic crystal fiber. *Opt. Express.* 25, 20313 (2017). <https://doi.org/10.1364/oe.25.020313>

Ziblat, R., Lirtsman, V., Davidov, D., Aroeti, B.: Infrared surface plasmon resonance: A novel tool for real time sensing of variations in living cells. *Biophys. J.* 90, 2592–2599 (2006). <https://doi.org/10.1529/biophysj.105.072090>

Figures

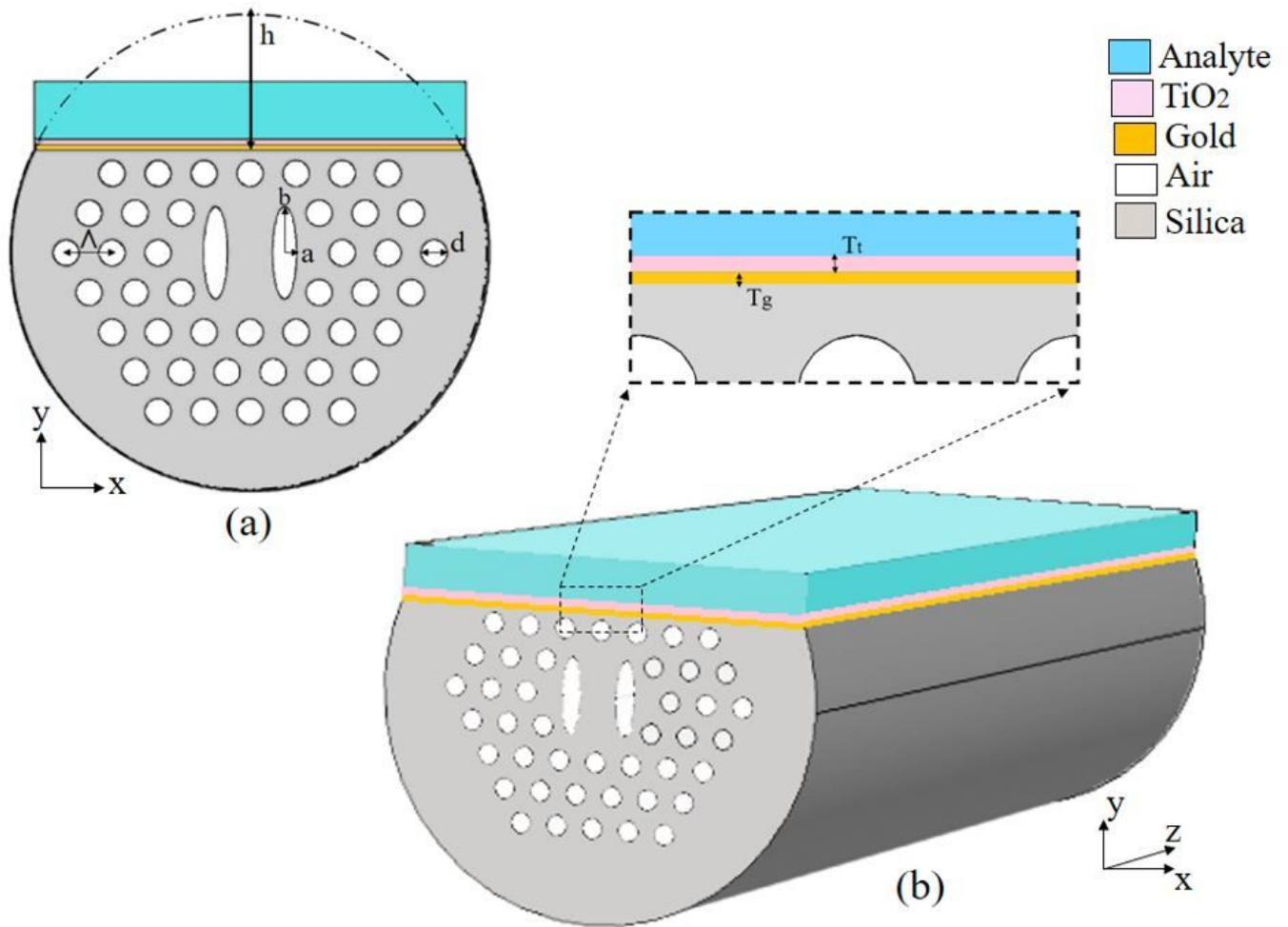


Figure 1

(a) Schematic of the proposed HB-D-PCF; (b) 3D view of the HB-D-PCF sensor

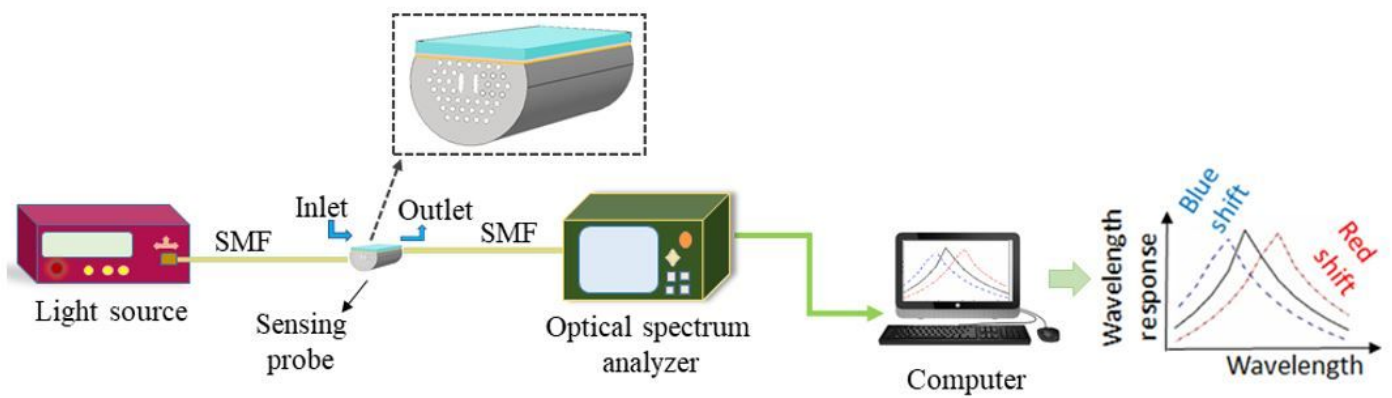


Figure 2

Schematic diagram of the proposed experimental setup

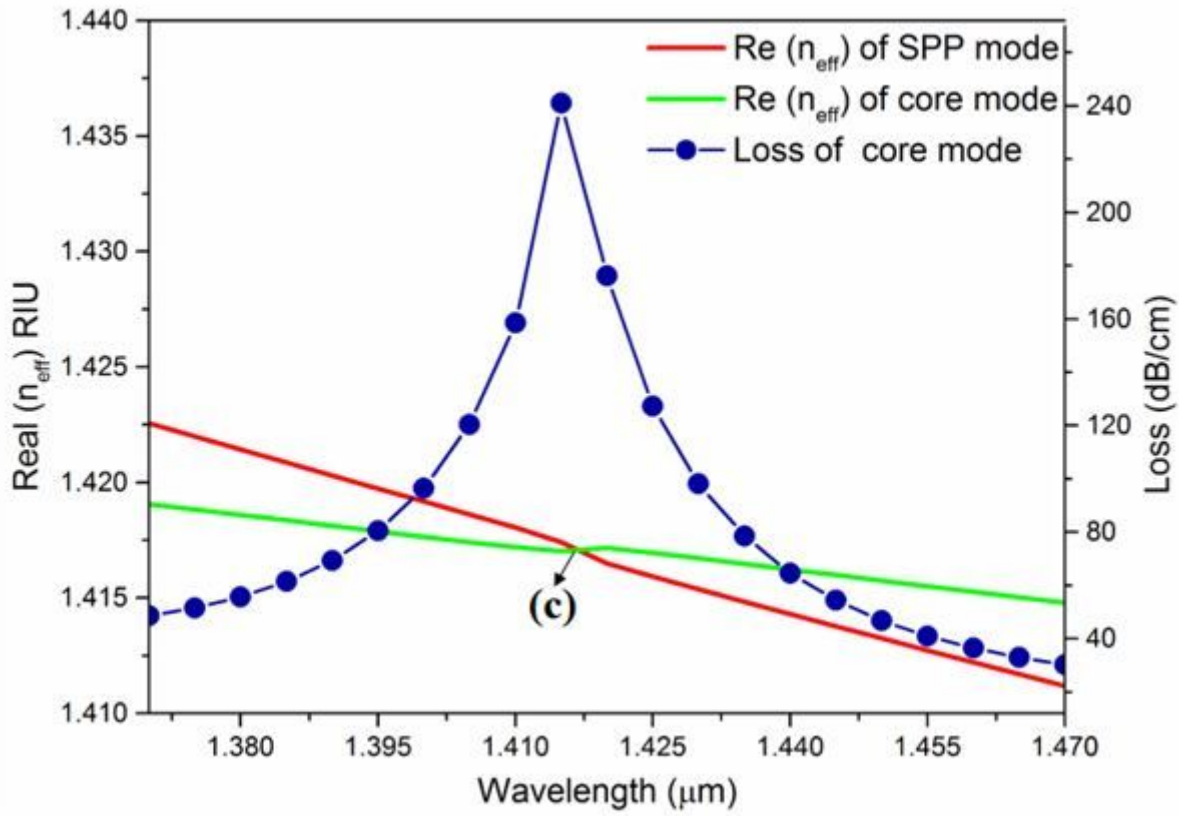


Figure 3

Dispersion relations of core mode and SPP mode for designed HB-D-PCF for $n_a=1.33$.

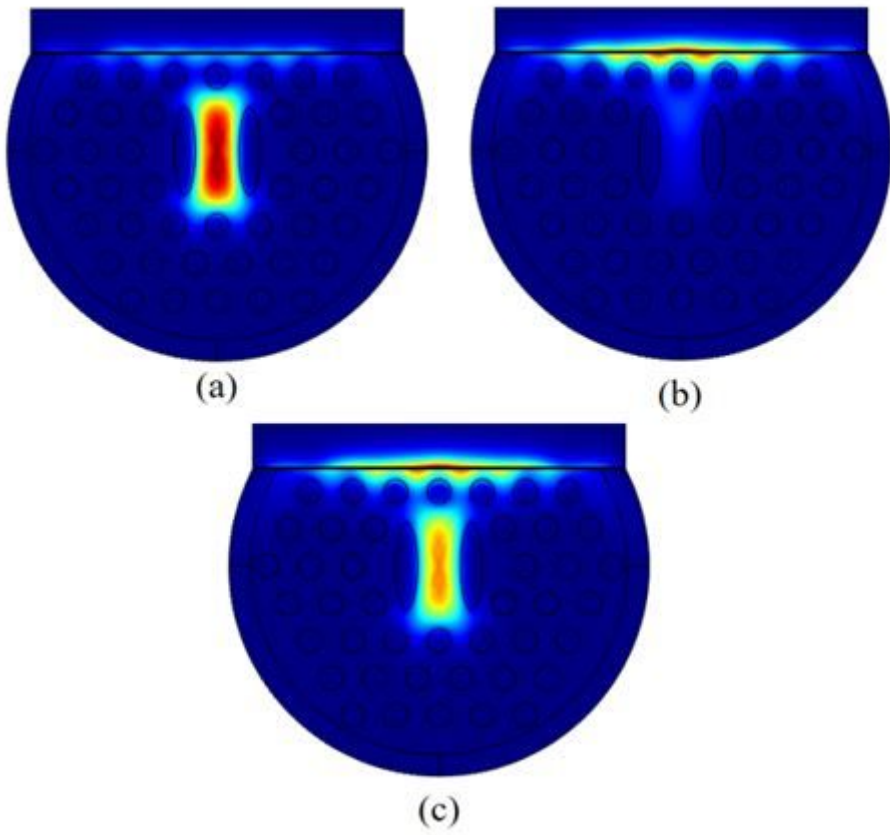


Figure 4

electric field distribution of (a) core guided mode, (b) SPP mode and (c) coupled mode.

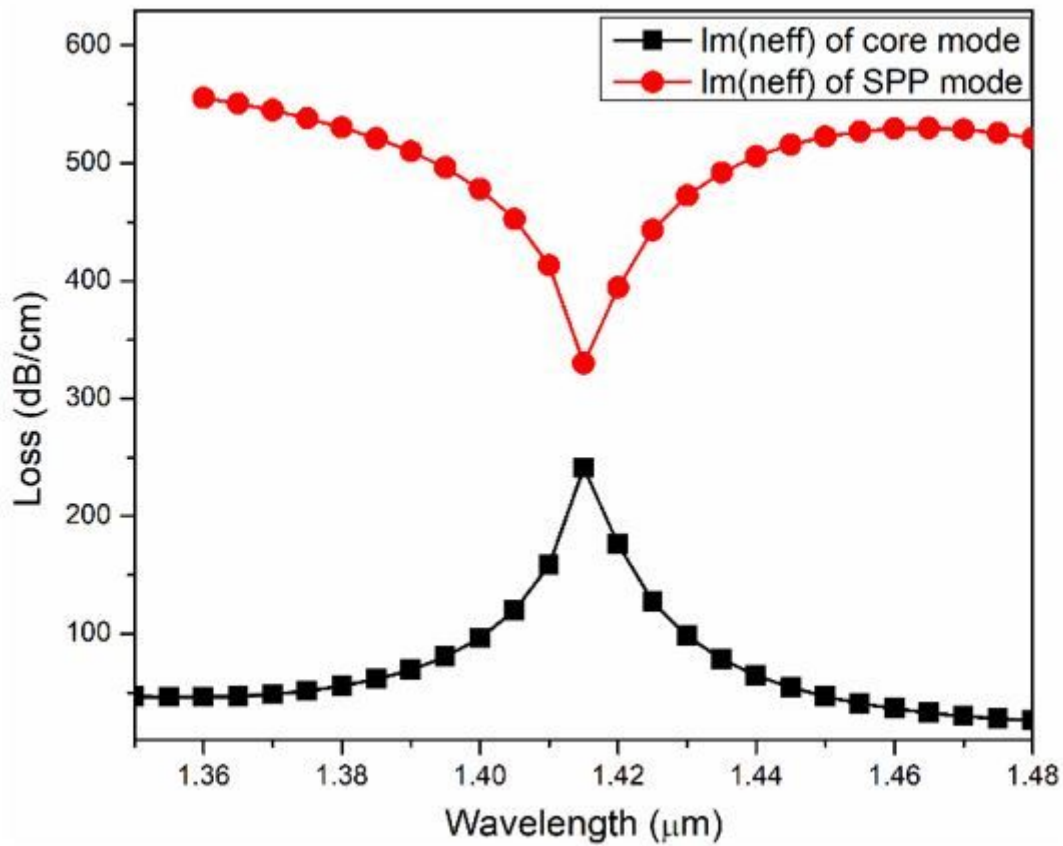


Figure 5

Incomplete coupling of core mode and SPP mode for the designed HB-D-PCF for $n_a=1.33$

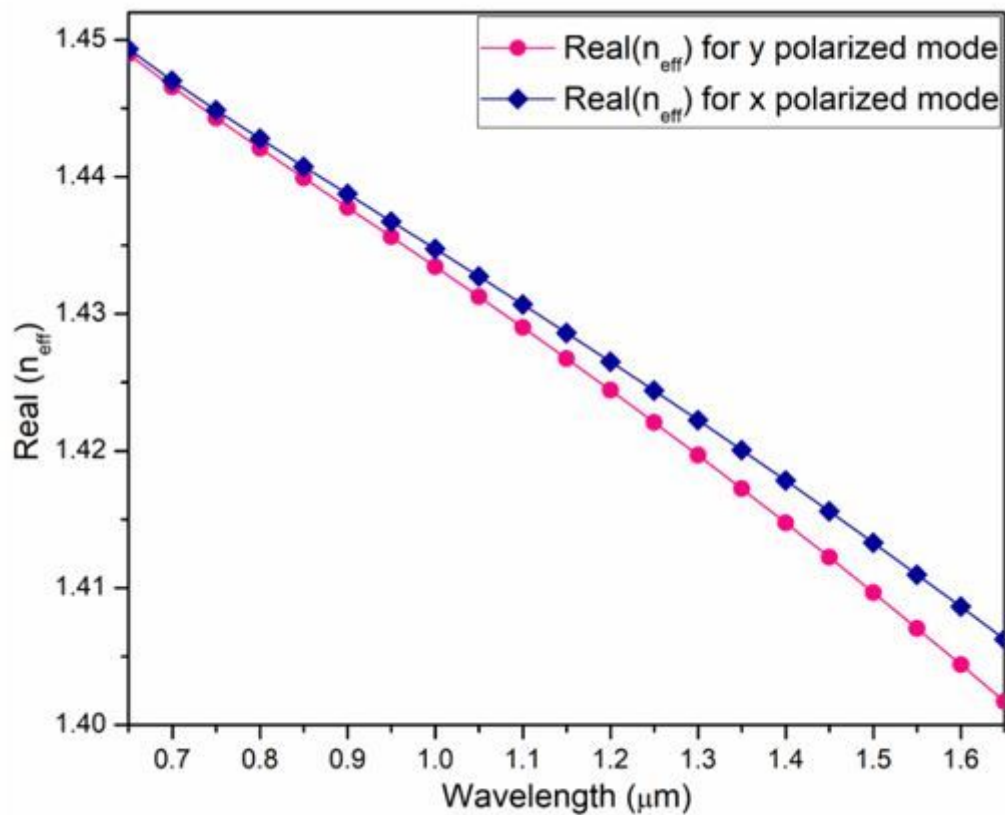


Figure 6

Real (n_{eff}) variation for both x and y polarized mode with changing wavelength for optimized unpolished PCF structure (De and Singh 2019a)

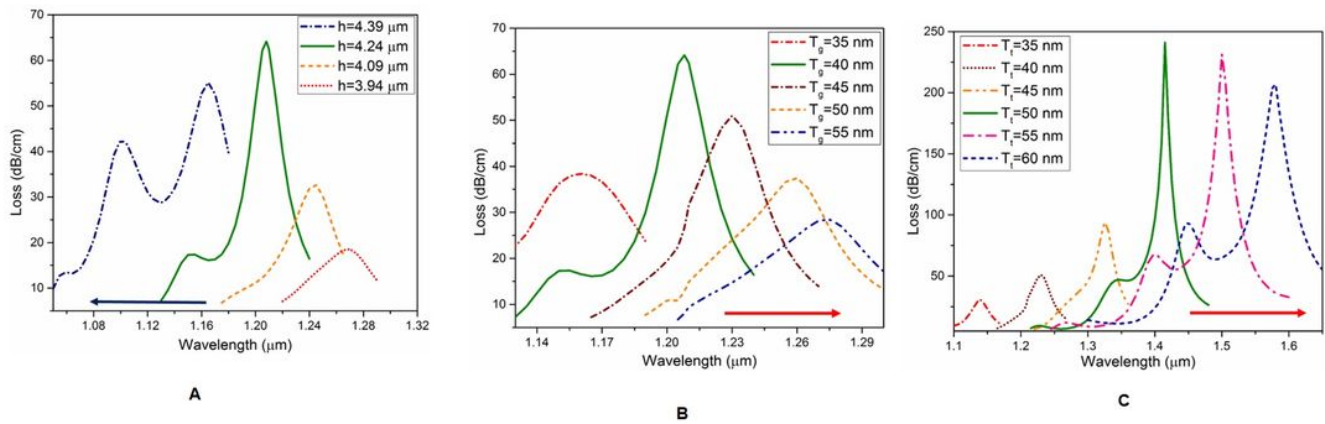


Figure 7

(a) Loss spectrum of the designed HB-D-PCF sensor with changing h at $n_a=1.33$. Loss spectrum of the designed HB-D-PCF sensor with changing (b) T_g and (c) T_t at $n_a=1.33$.

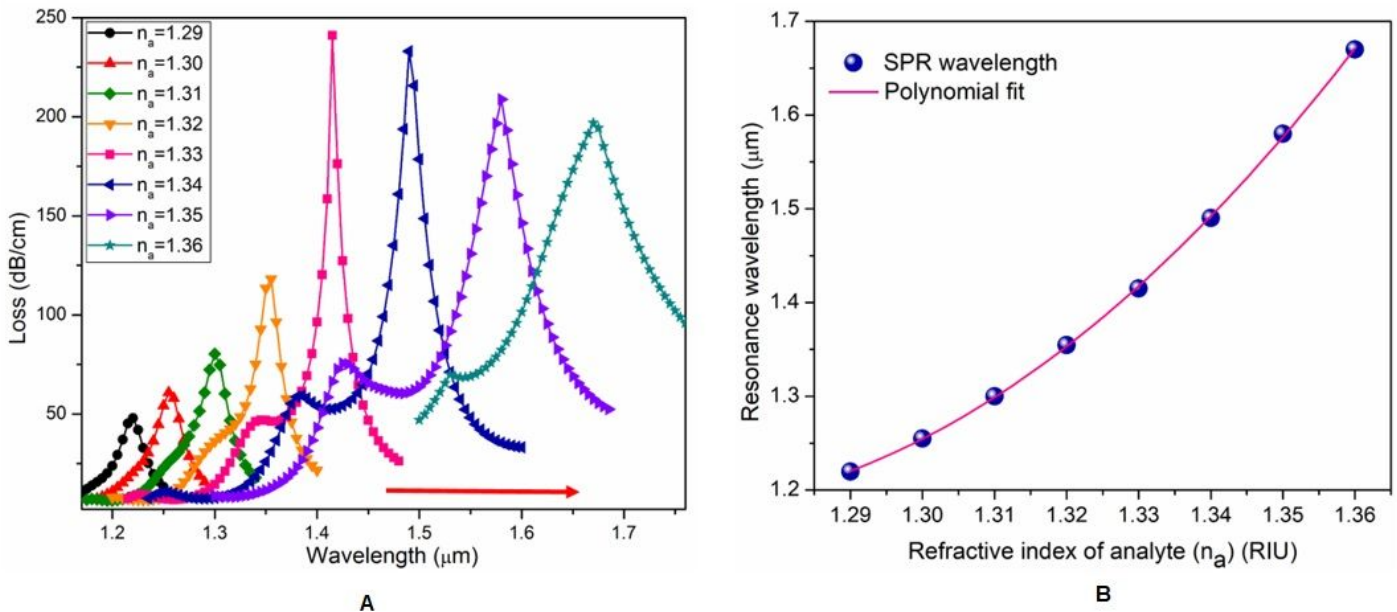


Figure 8

(a) Loss spectrum for various analytes, (b) SPR wavelength variation with changing analyte.

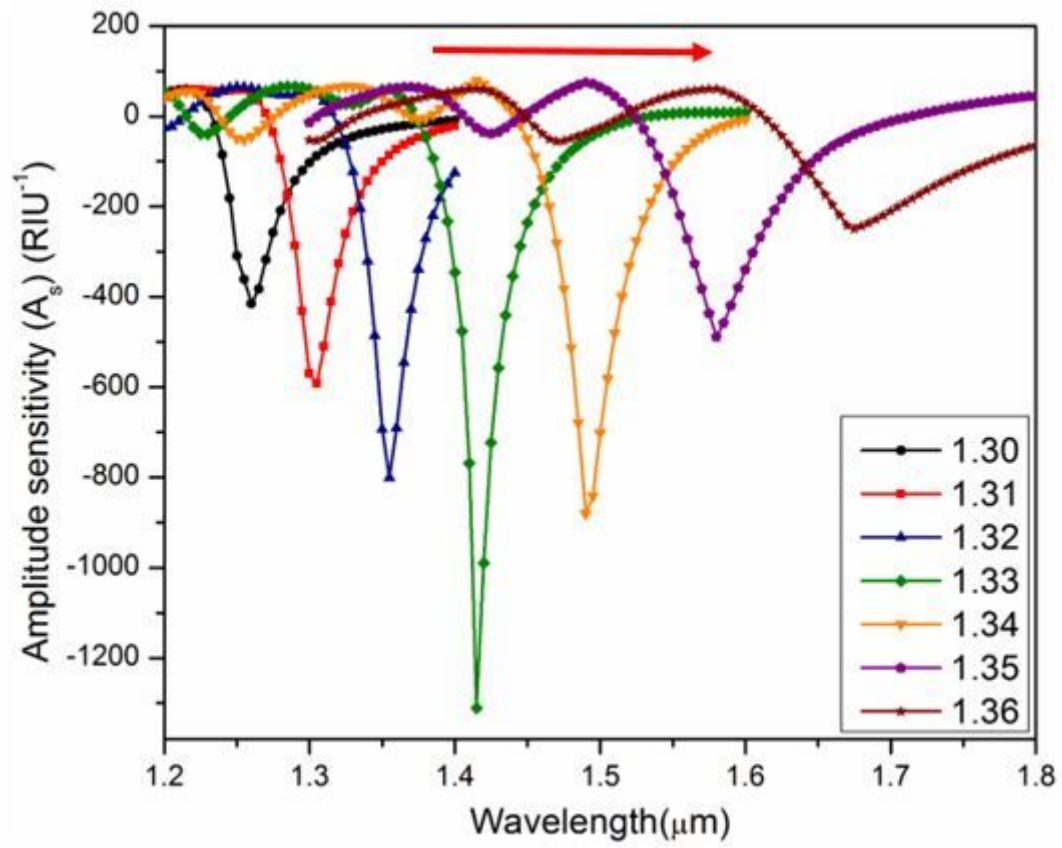


Figure 9

Amplitude sensitivity of proposed HB-D-PCF sensor with varying analyte

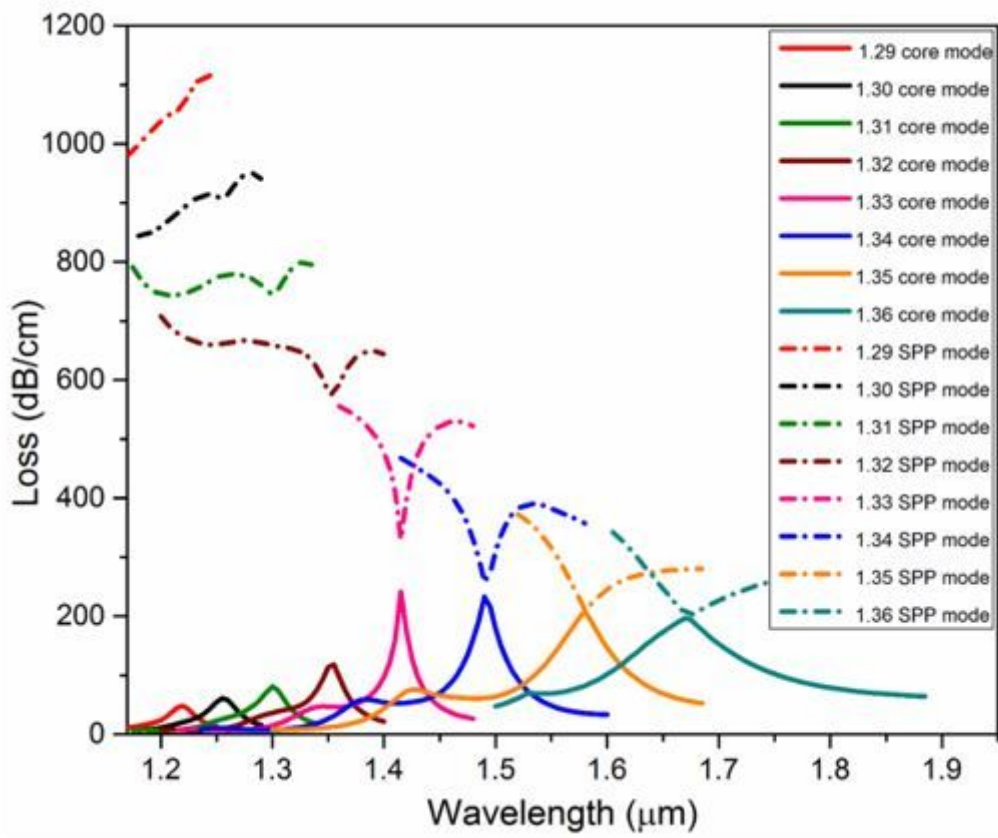


Figure 10

Coupling nature in RI range 1.29-1.36.